

Rapid Construction of Fe–Co–Ni Composition–Phase Map by Combinatorial Materials Chip Approach

Hui Xing,^{†,‡} Bingbing Zhao,^{†,‡} Yujie Wang,^{†,§} Xiaoyi Zhang,^{||} Yang Ren,^{||} Ningning Yan,[⊥] Tieren Gao,[#] Jindong Li,^{†,§} Lanting Zhang,^{*,†,‡,||} and Hong Wang^{†,‡,⊥}

[†]Materials Genome Initiative Center, Shanghai Jiao Tong University, Shanghai 200240, China

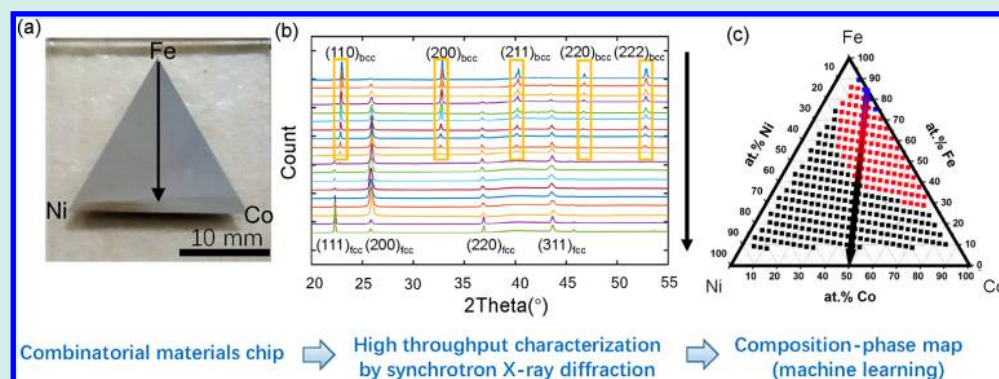
[‡]School of Materials Science and Engineering, Shanghai Jiao Tong University, Shanghai 200240, China

[§]Department of Physics and Astronomy, Shanghai Jiao Tong University, Shanghai 200240, China

^{||}X-ray Science Division, Advanced Photon Source, Argonne National Laboratory, Argonne, Illinois 60439, United States

[⊥]China Building Materials Academy, Beijing 100024, China

[#]Department of Materials Science and Engineering, University of Maryland, College Park, Maryland 20742, United States



ABSTRACT: One hundred nanometer thick Fe–Co–Ni material chips were prepared and isothermally annealed at 500, 600, and 700 °C, respectively. Pixel-by-pixel composition and structural mapping was performed by microbeam X-ray at synchrotron light source. Diffraction images were recorded at a rate of 1 pattern/s. The XRD patterns were automatically processed, phase-identified, and categorized by hierarchical clustering algorithm to construct the composition–phase map. The resulting maps are consistent with corresponding isothermal sections reported in the ASM Alloy Phase Diagram Database, verifying the effectiveness of the present approach in phase diagram construction.

KEYWORDS: combinatorial materials chip, Fe–Co–Ni, X-ray diffraction, hierarchical clustering, phase diagram

The conventional approach to phase diagram construction, featuring synthesis and characterization of one sample at a time, is costly, time-consuming, and unsystematic, which makes it less than satisfactory in the current era of accelerating technology. Since the 1960s,¹ attempts have been made to find more efficient ways to map the composition–phase relationship.² The combinatorial material chip technique, featuring high-throughput synthesis and rapid characterization of combinatorial library,^{3–7} has shown great potential to accelerate materials screening and optimization.^{8,9} Yoo et al. demonstrated in the Fe–Ni–Co ternary alloy system that it is feasible to map the complex relationship between crystal structure and composition using a thin film combinatorial materials chip containing continuous composition spread.^{10,11} Janghorban et al.¹² showed on a similar type of samples that a Cr–Ni–Re phase diagram at 1100 °C agrees well with the published phase diagram.

The throughput of structural mapping of a combinatorial library by X-ray diffraction (XRD) is largely affected by the flux and spot size of the X-ray beam. Synchrotron radiation, provides

an ideal X-ray source for rapid characterization with high spatial-resolution. Further acceleration can be achieved using a focused X-ray microbeam in combination with an area detector, which eliminates the time-consuming angular scan. It has been demonstrated that the diffraction patterns on combinatorial libraries can be acquired using synchrotron radiation with an exposure time between 1 and 30 s.¹³

To accommodate the large volume of data generated from high-throughput diffraction experiments, automatic routines for phase identification and clustering are required. Machine-learning methods were introduced in the data processing of diffraction spectra.^{5,14} For example, Bunn et al.¹⁵ adopted Adaboost feature learning, a supervised learning technique, in their analysis of phase formation and oxidation of Ni–Al thin films using XRD, Raman, and luminescence spectroscopy and

Received: November 12, 2017

Revised: January 9, 2018

Published: January 30, 2018

composition data. A disadvantage of this approach is the need for a fairly large training set, which is often unavailable in practice. Long et al.¹⁶ used non-negative matrix factorization (NMF), an unsupervised learning technique, for phase mapping to reduce the required data population, with minimal regard of underlying physics. Derivative approaches, such as CombiFD,¹⁷ GRENDEL,¹⁸ and AgileFD,¹⁹ were developed to ensure the resulting models carrying sufficient physical significance. Currently, the ability to tolerate peak position shift covering a wide range of compositions remains a challenge for phase mapping algorithms.

Clustering is a technique to sort data into groups according to certain measure. In a recent work, Iwasaki et al.⁶ compared the effectiveness of various dissimilar measures for hierarchical clustering analysis of X-ray diffraction data from combinatorial libraries. They found that the cosine, Pearson correlation coefficient and Jensen–Shannon divergence measures provide the best results in the presence of peak height change and a nonconstant position shift. By incorporating Gibbs' phase rule, physically meaningful phase maps of V–Mn–Nb oxide were constructed using AgileFD–Gibbs algorithm by Suram et al.²⁰

In this study, a systematic workflow for rapid construction of composition–phase map was developed, including preparation of combinatorial materials chip, structural and compositional characterization by synchrotron X-ray microbeam diffraction and X-ray fluorescence, and automatic data analysis based on hierarchical clustering techniques. A well-documented Fe–Co–Ni ternary system was chosen for demonstration purpose. The resulting composition–phase maps were compared with the isothermal sections in ASM Alloy Phase Diagram Database for confirmation.

The thin-film combinatorial materials chips, covering the entire composition range of Fe–Co–Ni ternary system, were deposited on quartz substrates using a custom-designed high-throughput combinatorial ion beam deposition system (HTC-IBD).²¹ Details of deposition procedure can be found in ref 21 (as shown in Figure 1a and b) and equilateral triangle

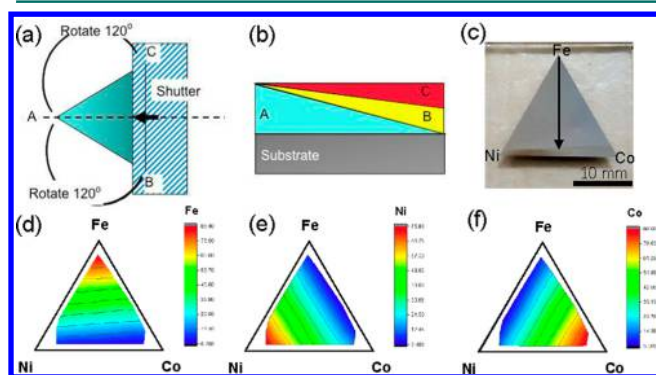


Figure 1. (a) Schematic illustration of the deposition procedure with a moving shutter.²¹ (b) Cross-section of the multilayered film with gradient composition spread.²¹ (c) A prepared Fe–Co–Ni equilateral triangle composition spread. XRF mappings of (d) Fe, (e) Ni, and (f) Co distribution of the composition spread (heat treated at 700 °C).

composition spreads were prepared (Figure 1c). The composition C_i (at. %) at each point on the chip is determined by the thickness of each component

$$C_i = \frac{t_i \rho_i / Z_i}{\sum_i t_i \rho_i / Z_i}, \quad \sum_i t_i = \text{const} \quad (1)$$

where t is the thickness, ρ is the density, and Z is the atomic weight of each component ($i = \text{Fe, Co, Ni}$ in the present case). The 100 nm thick multilayer films were sealed in evacuated quartz tubes and heat treated isothermally at 500, 600, and 700 °C for 2 h, respectively, followed by air quenching.

Mapping of chemical composition was carried out by microbeam X-ray fluorescence (XRF) spectroscopy on beamline 1–5 of the Stanford Synchrotron Radiation Light source (SSRL) at SLAC National Accelerator Laboratory with a step size of 2 mm. The results were calibrated with the wavelength dispersive X-ray spectroscopy (WDS) in an electron-probe microanalyzer (EPMA). Since the atomic weight and density of the three elements are close to each other, spatial distribution of Fe, Ni, and Co is rather linear as shown in Figure 1d–f, which is consistent with the design.

Pixel-by-pixel microbeam XRD mapping was conducted in reflection mode on beamline 11-ID-D of the Advanced Photon Source (APS) at Argonne National Laboratory. The measurement was done using an X-ray energy of 15.5 keV ($\lambda = 0.07999$ nm) at an incident angle of 15°. The beam was 45 (longitudinal direction) \times 100 (lateral direction) μm^2 with a photon flux $\sim 2 \times 10^{12}$ ph/s and the entire material chip was scanned with a step size of 600 μm . Good quality diffraction images were acquired using a low-background area detector (Pilatus3 2M, Dectris, Inc., Switzerland) at an exposure time of 1 s (Figure 2a), and then converted into 1D XRD patterns using FIT2D (Figure 2b). Around 400 diffraction patterns were recorded from the triangle region on each materials chip.

The lattice constants of the fcc and bcc phases from a pattern in the two-phase region (marked X in Figure 2c) were estimated to be 0.356 and 0.285 nm, respectively, comparable with the PDF card values of 0.3523 nm for fcc-Ni (no. 04-0850) and 0.2866 nm for bcc-Fe (no. 06-0696). Early studies indicated that alloying of Fe and Co into fcc-Ni resulted in an increased lattice constant,^{22–24} while the lattice constant of bcc-Fe first increased with adding up to ~ 25 at. % Co and then decreased with further increase in Co.²³ Therefore, the deviation in lattice constants from the pure metals is in qualitative agreement with the known trend of alloying.

Figure 2b displays XRD patterns obtained along a scan line from the Fe corner to the Ni–Co edge as shown in Figure 1c and 2c. Along the scan line, the pattern began with a bcc single phase, quickly evolved into a region of fcc and bcc phases coexisting and continued into an fcc single phase. Meanwhile, the individual peak positions shift slightly as a function of composition indicating the change in lattice constant. By manually grouping the patterns according to phases present, an Fe–Co–Ni composition–phase map at 600 °C was constructed (Figure 2c), which agrees well with the ASM Alloy Phase Diagram Database (Figure 4b).

To determine the phase regions automatically, hierarchical clustering analysis was adopted to group the diffraction patterns. Cosine metric was used to calculate the similarity index D between patterns (P_m, P_n) as follows:

$$D_{\text{cosine}}(P_m, P_n) = 1 - \frac{\sum_{i=1}^n (P_{m_i} \cdot P_{n_i})}{\sqrt{\sum_{i=1}^n P_{m_i}^2} \cdot \sqrt{\sum_{i=1}^n P_{n_i}^2}} \quad (2)$$

where P_{m_i} and P_{n_i} stand for i -th element of the vector P_m and P_n .

Figure 3a is a collection of all the XRD patterns scanned from the materials chip heat treated at 600 °C. Three strategies were used in clustering. First of all, the intensities at every diffraction

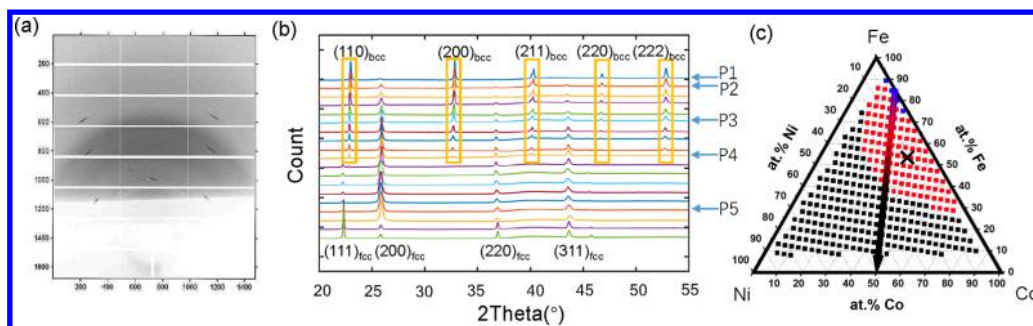


Figure 2. (a) Typical diffraction image with 1 s exposure time; (b) a group of converted XRD patterns following the scan line (shown in Figure 1c); (c) the manually constructed composition-phase map from the chip heat treated at 600 °C (blue dots, bcc; red dots, bcc + fcc; black dots, fcc).

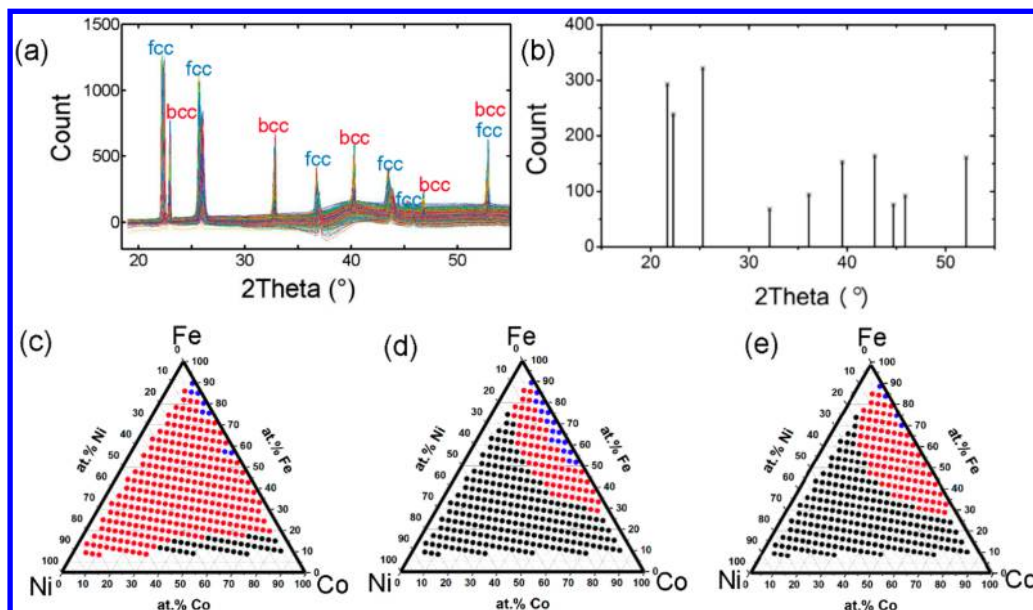


Figure 3. (a) Typical XRD patterns showing both fcc and bcc diffractions. (b) Peak positions and intensities identified from panel a. Composition-phase map by (c) clustering using full pattern strategy, (d) clustering using reduced pattern strategy, and (e) progressive clustering using reduced pattern strategy.

Table 1. Boolean Variable Table of Peak Positions and the Corresponding Similarity Index D According to Cosine Metric^a

peak (deg)	22.2 (fcc)	22.7 (bcc)	25.7 (fcc)	32.5 (bcc)	36.7 (fcc)	39.9 (bcc)	43.5 (fcc)	46.4 (bcc)	52.5 (fcc + bcc)	$D(P_i, P_n)$	fcc	bcc
P_1	0	1	0	1	0	1	0	1	1	0	0	1
P_2	0	1	1	1	0	1	0	1	1	0.09	1	1
P_3	1	1	1	1	1	1	1	1	1	0.26	1	1
P_4	1	1	1	0	1	0	1	0	0	0.80	1	1
P_5	1	0	1	0	1	0	1	0	0	1	1	0

^aThe last two columns are a result of automatic labeling.

angle were compared between the patterns (full pattern strategy) and three clusters were identified in the composition space (Figure 3c). Even though it does not violate Gibbs' phase rule, the size of the two phase region is drastically larger than the manually constructed map in Figure 2c. Such a huge discrepancy is primarily attributed to the nonconstant background in the full pattern (Figure 3a), causing high level of noise in the clustering analysis. In addition, peak shift and peak height change due to phase fraction are also recognized as major source for the misclustering.

Second, instead of the full pattern strategy, peak positions and heights were extracted from the patterns following the standard preprocessing procedure (Figure 3b). A list of discrete peak positions and intensities similar to ref 7 was generated for each

pattern. Depending on composition, the same diffraction peak taken from different location of the chip is likely to be located within a range of a nominal diffraction angle. The range of peak shift was determined by taking a histogram of the same peak in all the patterns. And the entire patterns were converted into a Boolean variable table including all the nominal peak positions of all the patterns, as exemplified in Table 1. The similarity index D was computed based on the Boolean vector P . As a result, clustering results using this reduced pattern strategy (Figure 3d) looked much more realistic compared with the full pattern strategy. 282 patterns out of 317 were correctly clustered (89.0%) with regard to the manual results, a significant improvement over the full pattern strategy.

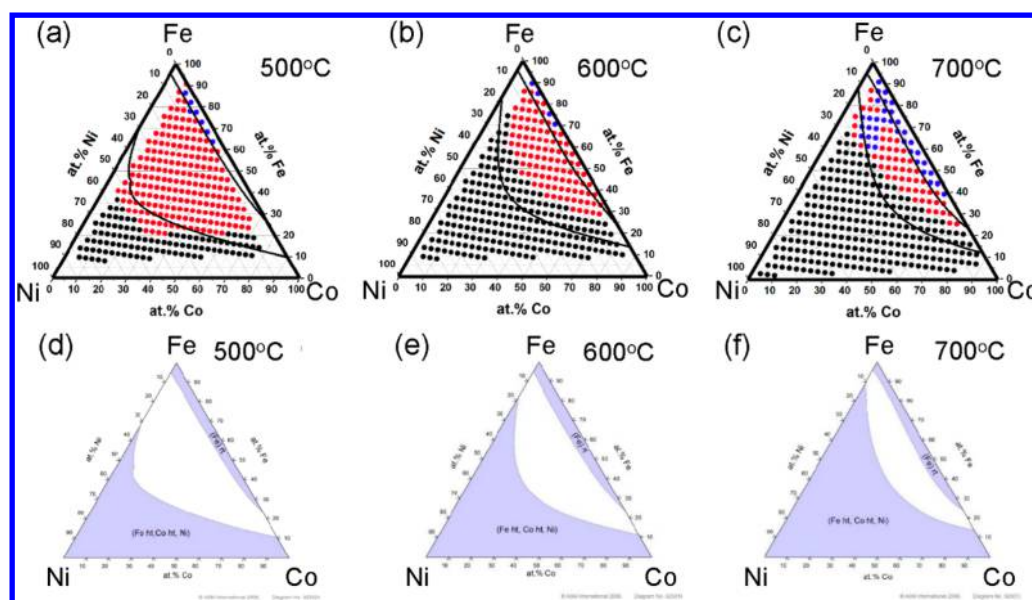


Figure 4. Constructed composition-phase maps of the materials chips heat treated at (a) 500 °C, (b) 600 °C, and (c) 700 °C (blue, bcc; red, bcc + fcc; black, fcc). (d–f) Isothermal sections of the Fe–Co–Ni system at the corresponding temperatures from ASM phase diagram Database for comparison (phase boundaries are superimposed to the corresponding maps of panels a–c).

Despite all the goodness, the reduced pattern strategy is far from perfect. Table 1 listed 5 vectors representing diffraction patterns from 5 typical areas: P_1 , P_3 , and P_5 were well within the bcc single phase, two-phase, and fcc single-phase regions, while P_2 and P_4 were both from the two-phase region, but near bcc and fcc single phase boundary (as indicated in Figure 2b), respectively. Since P_1 and P_5 had no peak in common, $D(P_1, P_5) = 1$, as expected. However, the similarity index between P_1 and the three vectors from two phase region ranged from 0.09 to 0.80, which gave rise quite large uncertainty in the clustering results since grouping decision relied solely on the D value. For example, P_2 was located near the bcc boundary just inside the two phase region so that it contained mainly bcc phase with fcc phase only beginning to emerge that there appeared only one fcc peak in the diffraction pattern. As a result, $D(P_1, P_2)$ was so small that P_2 had high probability being categorized as in the same group as P_1 . This explains that the area of bcc single phase region in Figure 3d was wider compared with that in Figure 2c.

To further increase the accuracy, an automatic phase labeling was carried out. By knowing which crystal structure each peak belongs to (indicated in the first row in Table 1), the pattern could be labeled as whether containing fcc structure or bcc structure or both (refer to the last two columns in Table 1). In this way, the small and incomplete peak set corresponding to the low content phase near the phase boundary cannot be ignored. As shown in Figure 3e, the clustering result based on reduced pattern strategy with phase labeling showed 310 patterns out of 317 were clustered correctly (97.8%), another significant increase in correctness.

The same work-flow was applied to other chips to construct composition-phase maps at 500 and 700 °C (Figure 4a and c). Compared with the manual identification results, 298 out of 306 (97.3%) and 312 out of 336 (92.9%) patterns were correctly clustered, respectively. Figure 4 compares the composition-phase maps from this work with the corresponding Fe–Co–Ni isothermal sections in the ASM Alloy Phase Diagram Database (Figures 4d–f). They were fairly consistent. The red-dotted two-phase region in the current composition-phase map expands with

decreasing heat treatment temperature. The few scattered blue dots in the red-dotted region in the composition-phase map at 700 °C were due to the weak fcc peaks in the patterns. These outliers can be removed by a subsequent human inspection.

Constructing composition-phase map by computer is a challenging task. In human analysis, the peak positions and intensities are extracted from a pattern and compared or indexed according to known knowledge, which is labor and knowledge intensive. In supervised machine learning approach, such as AutoPhase,¹⁵ human selected and labeled training data set is required to identify unique feature associated with the different phases. On the other hand, in unsupervised approaches such as NMF¹⁶ and clustering^{3–5} approaches, an appropriate feature extraction and incorporation of Gibbs' phase rule are important to render the results with physical information. Clustering is a relatively computationally efficient approach. However, the output using the full pattern strategy is likely to be dictated by the peak shift and noise in XRD patterns. To overcome this problem, the reduced pattern strategy, a two-step progressive process is proposed, which to a large extent mimics the process of human identification of an XRD pattern and satisfactory results are demonstrated. By reducing the dimension of data set in eq 1, it is also computationally favorable.

In summary, we use the Fe–Co–Ni system to demonstrate an integrated attempt to rapidly construct the composition-phase map. The isothermally heat treated 100 nm thick thin film materials chips were characterized by microbeam XRF and XRD at synchrotron light source. An exposure time of 1 s/pattern was achieved. A two-step progressive process based on hierarchical clustering was used for automated composition-phase map construction with average of over 95% correct rate. The resultant maps were consistent with those isothermal sections reported in the ASM Alloy Phase Diagram Database, verifying the effectiveness of the present approach. It is expected that this method is applicable to other material systems as well.

AUTHOR INFORMATION

ORCID

Xiaoyi Zhang: 0000-0001-9732-1449

Tieren Gao: 0000-0003-3404-6093

Lanting Zhang: 0000-0003-2547-1952

Notes

The authors declare no competing financial interest.

ACKNOWLEDGMENTS

This work was supported in part by National Key Research and Development Program of China (Grant No. 2017YFB0701900), National High Technology Research and Development Program of China (Grant No. SS2015AA034204), and the Science and Technology Commission of Shanghai Municipality (Grant Nos. 15DZ2260303 and 16DZ2260602).

REFERENCES

- (1) Kennedy, K.; Stefansky, T.; Davy, G.; Zackay, V. F.; Parker, E. R. Rapid Method for Determining Ternary - Alloy Phase Diagrams. *J. Appl. Phys.* **1965**, *36* (12), 3808–3810.
- (2) Wong-Ng, W. Evaluation of the Current Status of the Combinatorial Approach for the Study of Phase Diagrams. *J. Res. Natl. Inst. Stand Technol.* **2012**, *117*, 304–27.
- (3) Lebras, R.; Damoulas, T.; Gregoire, J. M.; Sabharwal, A.; Gomes, C. P.; van Dover, R. B. Constraint reasoning and Kernel clustering for pattern decomposition with scaling. *Principles and Practice of Constraint Programming—CP 2011* **2011**, 6876, 508–522.
- (4) Long, C. J.; Hattricksimpers, J.; Murakami, M.; Srivastava, R. C.; Takeuchi, I.; Karen, V. L.; Li, X. Rapid structural mapping of ternary metallic alloy systems using the combinatorial approach and cluster analysis. *Rev. Sci. Instrum.* **2007**, *78* (7), 072217.
- (5) Kusne, A. G.; Gao, T.; Mehta, A.; Ke, L.; Nguyen, M. C.; Ho, K.-M.; Antropov, V.; Wang, C.-Z.; Kramer, M. J.; Long, C.; Takeuchi, I. On-the-fly machine-learning for high-throughput experiments: search for rare-earth-free permanent magnets. *Sci. Rep.* **2015**, *4*, 6367.
- (6) Iwasaki, Y.; Kusne, A. G.; Takeuchi, I. Comparison of dissimilarity measures for cluster analysis of X-ray diffraction data from combinatorial libraries. *npj Comput. Mater.* **2017**, *3* (1), 4.
- (7) LeBras, R.; Damoulas, T.; Gregoire, J. M.; Sabharwal, A.; Gomes, C. P.; van Dover, R. B. Constraint Reasoning and Kernel Clustering for Pattern Decomposition with Scaling. *Principles and Practice of Constraint Programming—CP 2011* **2011**, 6876, 508–522.
- (8) Xiang, X. D.; Sun, X.; Briceño, G.; Lou, Y.; Wang, K. A.; Chang, H.; Wallacefreedman, W. G.; Chen, S. W.; Schultz, P. G. A combinatorial approach to materials discovery. *Science* **1995**, *268* (5218), 1738.
- (9) Xiang, X. D. Mapping of physical properties—composition phase diagrams of complex material systems using continuous composition material chips. *Appl. Surf. Sci.* **2002**, *189* (3–4), 188–195.
- (10) Yoo, Y. K.; Ohnishi, T.; Wang, G.; Duewer, F.; Xiang, X. D.; Chu, Y. S.; Mancini, D. C.; Li, Y.-Q.; O'Handley, R. C. Continuous mapping of structure–property relations in Fe1–xNi metallic alloys fabricated by combinatorial synthesis. *Intermetallics* **2001**, *9* (7), 541–545.
- (11) Yoo, Y. K.; Xue, Q.; Chu, Y. S.; Xu, S.; Hangen, U.; Lee, H.-C.; Stein, W.; Xiang, X.-D. Identification of amorphous phases in the Fe–Ni–Co ternary alloy system using continuous phase diagram material chips. *Intermetallics* **2006**, *14* (3), 241–247.
- (12) Janghorban, A.; Pfitzing-Micklich, J.; Frenzel, J.; Ludwig, A. Investigation of the Thin-Film Phase Diagram of the Cr–Ni–Re System by High-Throughput Experimentation. *Adv. Eng. Mater.* **2014**, *16* (5), 588–593.
- (13) Gregoire, J. M.; Van Campen, D. G.; Miller, C. E.; Jones, R. J. R.; Suram, S. K.; Mehta, A. High-throughput synchrotron X-ray diffraction for combinatorial phase mapping. *J. Synchrotron Radiat.* **2014**, *21* (6), 1262–1268.
- (14) Kusne, A. G.; Keller, D.; Anderson, A.; Zaban, A.; Takeuchi, I. High-throughput determination of structural phase diagram and constituent phases using GRENDL. *Nanotechnology* **2015**, *26* (44), 444002.
- (15) Bunn, J. K.; Han, S.; Zhang, Y.; Tong, Y.; Hu, J.; Hattrick-Simpers, J. R. Generalized machine learning technique for automatic phase attribution in time variant high-throughput experimental studies. *J. Mater. Res.* **2015**, *30* (7), 879–889.
- (16) Long, C. J.; Bunker, D.; Li, X.; Karen, V. L.; Takeuchi, I. Rapid identification of structural phases in combinatorial thin-film libraries using x-ray diffraction and non-negative matrix factorization. *Rev. Sci. Instrum.* **2009**, *80* (10), 103902.
- (17) Ermon, S.; Le Bras, R.; Suram, S. K.; Gregoire, J. M.; Gomes, C.; Selman, B.; van Dover, R. B. Pattern Decomposition with Complex Combinatorial Constraints: Application to Materials Discovery. *AAAI'15 Proceedings of the Twenty-Ninth Conference on Artificial Intelligence (AAAI-15)* **2015**, 636–643.
- (18) Massoudifar, P.; Rangarajan, A.; Zare, A.; Gader, P. An Integrated Graph Cuts Segmentation and Piece-Wise Convex Unmixing Approach for Hyperspectral Imaging. *2014 6th Workshop on Hyperspectral Image and Signal Processing: Evolution in Remote Sensing (WHISPERS)* **2014**, 442–444.
- (19) Suram, S. K.; Xue, Y.; Bai, J.; Le Bras, R.; Rappazzo, B.; Bernstein, R.; Bjorck, J.; Zhou, L.; van Dover, R. B.; Gomes, C. P.; Gregoire, J. M. Automated Phase Mapping with AgileFD and its Application to Light Absorber Discovery in the V–Mn–Nb Oxide System. *ACS Comb. Sci.* **2017**, *19* (1), 37–46.
- (20) Suram, S. K.; Xue, Y.; Bai, J.; Le Bras, R.; Rappazzo, B.; Bernstein, R.; Bjorck, J.; Zhou, L.; van Dover, R. B.; Gomes, C. P.; Gregoire, J. M. Automated Phase Mapping with AgileFD and its Application to Light Absorber Discovery in the V–Mn–Nb Oxide System. *ACS Comb. Sci.* **2017**, *19* (1), 37–46.
- (21) Xiang, X.-D.; Wang, G.; Zhang, X.; Xiang, Y.; Wang, H. Individualized Pixel Synthesis and Characterization of Combinatorial Materials Chips. *Engineering* **2015**, *1* (2), 225–233.
- (22) Cameron, A. R. R. E. N. Kamacite and taenite superstructures and a metastable tetragonal phase in iron meteorites. *Am. Mineral.* **1966**, *51*, 37–55.
- (23) Pearson, W. B. *A Handbook of Lattice Spacings and Structures of Metals and Alloys*; Pergamon Press, 1958; p 504–506.
- (24) Lupi, C.; Dell'Era, A.; Pasquali, M.; Imperatori, P. Composition, morphology, structural aspects and electrochemical properties of Ni–Co alloy coatings. *Surf. Coat. Technol.* **2011**, *205* (23–24), 5394–5399.